International Journal of Design & Nature and Ecodynamics
Vol. 21, No. 5, May, 2026, pp. 1387-1395
Journal homepage: http://iieta.org/journals/ijdne

CTAC-Assisted Hydrothermal Synthesis of $BaCO_3$ Nanostructures: Structural, Morphological, and Property Evaluation

Marwa A. Anber[1*], Anwar Qasim Saeed[2], Ali A. Turki Aldalawi[2]

[1] Department of Material Engineering, College of Engineering, Mustansiriyah University, Baghdad 14022, Iraq
[2] Department of Vocational Education of Babylon, Ministry of Education, Babylon 51001, Iraq

Corresponding Author Email: marwa3nber@uomustansiriyah.edu.iq

https://doi.org/10.18280/ijdne.210515

Received: 14 February 2026
Revised: 17 April 2026
Accepted: 24 April 2026
Available online: 31 May 2026

Keywords:
barium carbonate, Cetrimonium chloride, surfactant, morphology, crystallite size reduction

ABSTRACT

Barium carbonate ($BaCO_3$) nanostructures were synthesised by a hydrothermal route in the absence and presence of cetyltrimethylammonium chloride (CTAC) as a cationic surfactant, and the resulting powders were examined by X-ray diffraction (XRD), Fourier-transform infrared spectroscopy (FTIR), and field-emission scanning electron microscopy (FE-SEM). Single-peak Scherrer analysis applied to the most intense reflection yielded crystallite sizes of approximately 94 nm and 55 nm for the surfactant-free and CTAC-treated samples, respectively, while averaging over the ten strongest reflections gave 43 nm and 34 nm. To remove the bias associated with selecting a single peak, the diffraction patterns were further analysed by Williamson–Hall and size–strain (Halder–Wagner) treatments, which converged on D ≈ 75 nm and ≈ 21 nm and on D ≈ 32 nm and ≈ 19 nm for the two samples, respectively. Least-squares refinement of the orthorhombic witherite cell (Pmcn) returned a = 5.287 to 5.317 Å, b = 8.926 to 8.905 Å, and c = 6.446 to 6.453 Å, indicating an anisotropic surface strain rather than a uniform cell expansion. A Harris texture analysis showed a marked preferential growth on the (111) plane (TC ≈ 6.5) for the CTAC sample. The carbonate vibrations observed at 1440, 860, and 690 cm^{-1} in both samples were verified by the FTIR data. Scientists concluded that the slight intensity variations in the data were caused by the interaction between carbonate chemicals and surfactants. The surfactant-free powder had irregular agglomerates, which transformed into plate-like crystallites that retained limited agglomeration in the CTAC-treated powder, according to the FE-SEM pictures. The combined microstructural image shows that, under the current hydrothermal conditions, CTAC works through two processes: enhanced nucleation and isotropic surface inhibition. Scientists believe that the resulting $BaCO_3$ powder, which has well-organized tiny particles, is a perfect precursor for functional applications in the future.

1. INTRODUCTION

Barium carbonate ($BaCO_3$) exists as an inorganic compound that people identify using the chemical symbol, and which multiple industrial applications use throughout glass and ceramics manufacturing and optical material production because of its chemical composition stability and various beneficial properties [1-3]. Many techniques are based on the properties of this material. The modern interest in this material is due to its ability to convert $BaCO_3$ (which is what is always made when preparing barium titanate) into barium titanate, with the attendant benefits of, for example, improved dielectric constant, which leads to improved performance in electronic devices [4, 5]. Cetyltrimethylammonium chloride (CTAC) or Cetrimonium chloride, an organic compound, is vital for various uses because it behaves like a surfactant, thereby enhancing the characteristics of nanomaterials. Initial research has indicated that nanomaterials' crystal shapes can be improved through the addition. Research by Inam et al. [6] confirmed the role of surfactants in the structural properties of nanomaterials, resulting in wider size ranges and uniform particle homogeneity. Moon et al. discovered that the incorporation of the cationic surfactant Cetrimonium bromide (CTAB) into ceramic nanomaterials can allow very precise control of nanoparticle size and shape and thus enable the realization of many designs by adjusting the speed and regulating the reaction period in the mixing stage during synthesis [7]. In order to improve ZnO nanoparticle dispersion and increase their use for electronic applications, Zhang et al. [8] employed a surfactant. Chen et al. [9] proposed that CTAC may be utilized to improve the surface morphology and homogeneity of silica nanoparticle crystals, a similar outcome to what other researchers had obtained by employing CTAC to improve the characteristics of nanoceramics [9]. Also, in other research, it has been proven that adding a surfactant to nano-ceramics works to enhance the monodispersing of nanoparticles and increase the sensitivity of the thermistor in the low temperature range, as demonstrated by the improvement of temperature-dependent electrical resistance behavior [10]. CTAB was applied to nanoparticles in the

reverse micelle technique, and colloidal gold nanocrystals were produced, from which self-assembled superlattices improved their stability and dispersion property [11, 12]. Several methods have been used to synthesize nanostructures. Shahid et al. [13] reported that this method can produce $BaCO_3$ in different forms such as rods, needle-like particles, and flower-shaped structures. They also observed that the final shape depends on factors like reaction time and the amount of nickel added during preparation. This shows that the CHM method is a useful way to control the structure of $BaCO_3$ for applications such as sensors and catalytic materials. Mishra et al. [14] showed that CTAB improves particle dispersion of ZnO nanoparticles through morphology control, and Ohkubo et al. [15] used CTAB-containing surfactant assemblies that served as soft templates for mesoporous silica particles, enabling tunable pore size and controllable hexagonal-to-lamellar mesostructure. CTAB and CTAC belong to the same family of cationic surfactants. They have the same C16 alkyl tail and the same trimethylammonium head, and they differ only in the counter-ion (Cl^- for CTAC and Br^- for CTAB). The two surfactants show different behavior in water despite having only one chemical difference. The critical micelle concentration of CTAC at 25 ℃ is between 1.1 and 1.6 mM, which is a little higher than the published value of 0.9–1.0 mM for CTAB [16-18]. This is because, in contrast to Cl^-, Br^- forms a stronger connection with the cationic head group. While CTAC micelles retain their loose structure with mostly spherical form, CTAB micelles become more compact as they evolve into rod-shaped structures because a closely bonded counter-ion inhibits the electrostatic forces that exist between neighboring head groups [19, 20]. When these surfactants adsorb on a solid surface, the same result is seen: CTAB forms compact, well-ordered bilayers that can act as relatively rigid templates, while the CTAC layer moves more, making it easier for ions from the surrounding solution to reach the carbonate group on the crystal surface [21]. Researchers have employed CTAB to create anisotropic gold nanorods [12, 18] and ordered mesoporous silicas [10, 15], whereas CTAC is more effective at extracting CO_3^{2-} anions on micelle surfaces and increasing nucleation without creating a primary crystal shape [9, 16, 22]. $BaCO_3$ nanoparticles have an impact on the polarization resistance of composite cathodes used in ceramic fuel cells, as demonstrated by Desta et al. [23]. Two-dimensional sheet-like structures offer superior surface area and active site density benefits for their applications, as Zavabeti et al. [24] showed. The researchers found that choosing the right surfactant was necessary to regulate the nucleation and growth processes. For these reasons, the researchers used CTAC surfactant for their investigation. $BaCO_3$ nanostructures have been analyzed using Fourier-transform infrared spectroscopy (FTIR) and X-ray diffraction (XRD) techniques to determine their structural and chemical changes under CTAC additives. It has been shown that the addition of surfactants has an effect on the chemical and structural nature. The research discussed how $BaCO_3$ nanoparticles were affected by CTAC using XRD analysis, FTIR spectroscopy, and field-emission scanning electron microscopy. Through these investigations, modifications within the crystallography as well as surface morphology were revealed when exposed to CTAC. Moreover, the research aimed to develop the properties of $BaCO_3$ for forthcoming use in the synthesis of barium titanate and make it more suitable for various fields.

2. EXPERIMENTAL

2.1 Preparation of barium carbonate

The production of $BaCO_3$ nanostructure involved a hydrothermal method. Barium chloride ($BaCl_2$, Kishida Chemical), sodium bicarbonate ($NaHCO_3$; Solvay), and sodium hydroxide (NaOH; Nacalai Tesque, 98%) were used to make the precursor. A 25 ℃ temperature was used to produce a combination of 1 M $BaCl_2$ (15 mL aqueous solution) and 1 M $NaHCO_3$ (10 mL aqueous solution). Next, 2 M NaOH and 5 mL of ethylene glycol (EG) solution were added, either with or without the addition of 0.1 g CTAC aqueous solution in 5 mL of deionized (DI) water. We used 0.1 g of CTAC in 5 mL of water, giving a final concentration of 6.25 mM in the reaction mixture. This is higher than the CMC of CTAC in water at 25 (1.1 mM) [16, 17], so micelles can form. The micelles contribute to regulating the development of $BaCO_3$ crystals while reducing random precipitation. To guarantee the production of well-crystallized $BaCO_3$, the reaction conditions (200 ℃, 20 h) were employed [13]. After the hydrothermal process, the product was separated using a centrifuge, and it was thereafter repeatedly cleaned in distilled water and dried at 70 ℃. Eq. (1) depicts the reactant and end product reaction flow.

$$BaCl_2.2H_20 + 2NaOH + NaHCO_3 = 2NaCl + 2H_2O \quad (1)$$

2.2 Characterization

The synthesized $BaCO_3$ was analyzed by XRD (ELIS, PHILIPS-binary scan), Field emission scanning electron microscopy (FE-SEM, AxiaChemi-SEM), and FTIR spectroscopy (Nicolet IS50). The crystalline nanostructure of $BaCO_3$ prepared by the hydrothermal method was characterized using Cu-Kα radiation (35 kV, 30 mA) in XRD measurements at 25 ℃ temperature. XRD analysis was used to estimate the lattice parameters of the a and c-axes from the (200) and (111) planes. The morphology and form of the produced $BaCO_3$ were examined using FE-SEM.

3. RESULTS AND DISCUSSION

3.1 Fourier-transform infrared spectroscopy analysis of barium carbonate samples

$BaCO_3$ samples were analysed using FTIR spectroscopy to study the effect of CTAC on the functional groups (see Figure 1(a)). A band observed at 1440 cm^{-1} is assigned to the asymmetric stretching vibration of the carbonate group (CO_3^{2-}). After adding CTAC, a noticeable change in the intensity of this band was observed, suggesting a possible surface interaction between CTAC molecules and the carbonate species. The band at 860 cm^{-1}, related to out-of-plane bending vibrations, also shows a variation in intensity after CTAC addition, indicating a change in the local environment of the carbonate groups. The band at 690 cm^{-1} corresponds to in-plane bending vibrations of the carbonate group. A weak band around 1067 cm^{-1} may be attributed to additional carbonate-related vibrational modes. In addition, the characteristic vibration at 2836 cm^{-1}, assigned to C–H stretching vibrations, points towards the presence of CTAC on

the surface of barium carbonate nanostructures [25].

3.2 X-ray diffraction study of structure and crystallite size

The XRD in the presence and absence of CTAC in $BaCO_3$, and the comparison between the patterns obtained, is displayed in Figure 1(b). XRD data showed that the presence of CTAC transformed the crystalline patterns. The peak intensity at 27.5°, which matched the (002) level of $BaCO_3$, showed improved crystal structure organization because there were fewer defects in the material. Furthermore, variations in the intensity values of the peaks seen at 23.2°, 24.7°, and 29.4°, which correspond to planes (111), (200), and (201), respectively, indicate improved crystalline uniformity and crystal formation [26]. Stronger peaks are seen in the CTAC-containing sample than in the non-CTAC-containing sample. This indicates that the presence of CTAC enhances the crystallinity of $BaCO_3$. There is noticeable peak broadening in the pattern without CTAC, indicating random-sized crystal sizes or more defects in the crystal structure. In the presence of CTAC, the diffraction peaks are noticeably different, which is a direct consequence of the reduced crystallite size.

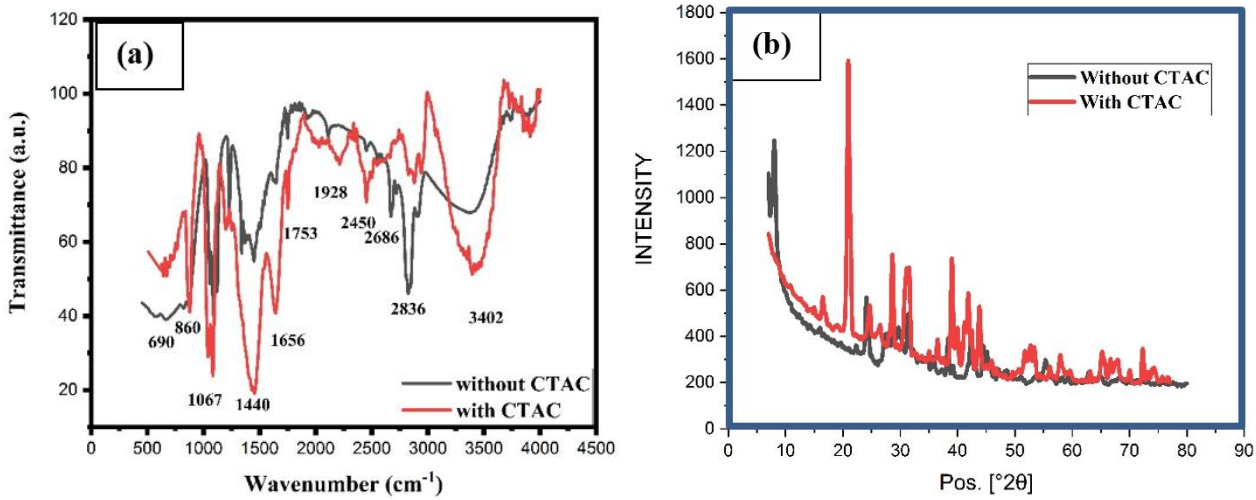

Figure 1. (a) The Fourier-transform infrared spectroscopy (FTIR) spectra of $BaCO_3$ in the presence of CTAC (red line) and in the absence of CTAC (black line), (b) The X-ray diffraction (XRD) analysis of $BaCO_3$ in the presence of CTAC and in the absence of CTAC

Notes: CTAC: Cetyltrimethylammonium chloride.

3.2.1 Single-peak Scherrer estimate

Crystallite size calculation: the broadening of XRD peaks may be used to determine crystallite sizes using the Scherrer Eq. (2):

$$D = \frac{K\lambda}{\beta cos\theta} \tag{2}$$

Hence, K is the shape factor (typically 0.9), D is the crystallite size, the wavelength (λ) of the X-ray radiation (Cu-Kα) is 0.15418 nm, the Bragg angle is represented by θ, and the peak's full width at half maximum (FWHM) is β in radians. By applying the Scherrer equation to the most intense peaks, we can compare the crystal sizes of $BaCO_3$ in the presence or absence of CTAC. The FWHM of the most intense $BaCO_3$ reflection at 2θ = 23.97° is 0.0866° (1.51×10^{-3} rad) for the surfactant-free sample, and the most intense reflection of the CTAC-treated sample at 2θ = 31.40° has a FWHM of 0.1515° (2.64×10^{-3} rad). With K = 0.9 and λ = 0.15418 nm, the Scherrer equation gives crystallite sizes of about 94 nm and 55 nm, respectively, for the most intense peaks, and average values of 43 nm and 34 nm when the ten most intense reflections of each pattern are averaged. CTAC therefore reduces the average crystallite size by roughly 20%, which is consistent with the adsorption of CTA^+ on the carbonate surface, limiting subsequent growth.

Worked example for the most intense reflection of the surfactant-free sample (2θ = 23.97°, FWHM = 0.0866°):

$$\theta = 11.985°, \cos\theta = 0.9782$$

$$\beta = 0.0866 \times \pi/180 = 1.512 \times 10^{-3} \text{ rad}$$

$$D_{without} = \frac{0.9 \times 0.1542}{1.512 \times 10^{-3} \times 0.9782} = 93.8 \text{ nm} \tag{3}$$

Worked example for the most intense reflection of the CTAC sample (2θ = 31.40°, FWHM = 0.1515°):

$$\theta = 15.70°, \cos\theta = 0.9627$$

$$\beta = 0.1515 \times \pi/180 = 2.644 \times 10^{-3} \text{ rad}$$

$$D_{with} = \frac{0.9 \times 0.1542}{2.644 \times 10^{-3} \times 0.9627} = 54.5 \text{ nm} \tag{4}$$

3.2.2 Williamson–Hall analysis

The Williamson–Hall (W–H) approach decomposes the total broadening of a Bragg peak into a size-related and a strain-related contribution by means of the uniform-deformation expression (Eq. (5)):

$$\beta cos\theta = \frac{k\lambda}{D} + 4\varepsilon sin\theta \tag{5}$$

where, ε is the average microstrain. The reflections used in the analysis were restricted to those with a relative intensity above 5% and a FWHM below 0.5°, and the $K\alpha_1/K\alpha_2$ split components were excluded. Plotting βcosθ against 4 εsinθ (Figure 2) and fitting a straight line by least squares yields a volume-averaged crystallite size of $D \approx 74.7$ nm for the surfactant-free sample and $D \approx 20.5$ nm for the CTAC sample, with microstrain values of $\varepsilon \approx +0.95 \times 10^{-3}$ and $\varepsilon \approx -0.69 \times 10^{-3}$, respectively. The poor fit quality ($R^2 \approx 0.066$) of the

Williamson–Hall plot indicates that the strain contribution to peak broadening is negligible and that the linear model is not well-constrained by the data. The W–H crystallite sizes (74.7 nm and 20.5 nm) should therefore be treated as indicative trend values rather than precise absolute measurements. The more reliable Halder–Wagner analysis (R^2 = 0.78–0.908) gives D ≈ 32 nm and ≈ 19 nm and is the preferred basis for quantitative comparisons in this work.

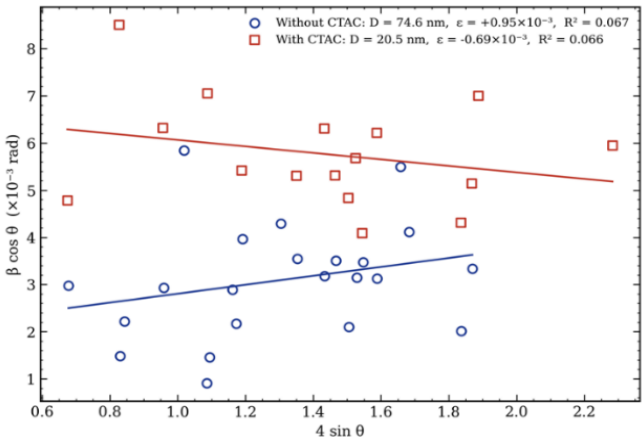

Figure 2. Williamson–Hall plot for the $BaCO_3$ samples synthesised without and with cetyltrimethylammonium chloride (CTAC)

Notes: The intercept of the linear fit gives the volume-averaged crystallite size *D*, and the slope gives the macrostrain *ε*.

3.2.3 Size–strain plot (Halder–Wagner)

Because the W–H plot can be unduly influenced by the weak, broad reflections, a second analysis was performed in the Halder–Wagner formulation, in which the size and strain contributions are separated according to Eq. (6):

$$(d\beta cos\theta)^2 = \left(\frac{k\lambda}{D}\right).d^2\beta cos\theta + (\frac{\varepsilon}{2})^2 \qquad (6)$$

Plotting $(d\beta cos\theta)^2$ against $d^2\ \beta cos\theta$ (Figure 3) returns a linear regression whose slope is proportional to 1/D and whose intercept is proportional to ε².

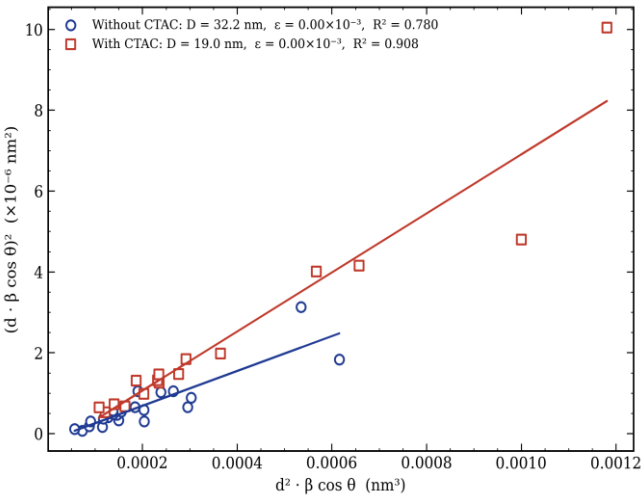

Figure 3. Size–strain plot of the two $BaCO_3$ samples in the Halder–Wagner representation

Notes: The slope of the linear fit gives the volume-averaged crystallite size *D*.

The fit is considerably more stable than the W–H plot (R^2 = 0.78 and 0.91 for the surfactant-free and the CTAC samples, respectively) and gives D ≈ 32.2 nm and D ≈ 19.0 nm, with a macrostrain that is essentially negligible in both samples. The size–strain estimate is therefore the most reliable absolute description of the average crystallite size in the present work, and the ratio between the two values (≈ 1.69) is in close agreement with the ratio of ≈ 1.71 obtained from the single-peak Scherrer estimate (94 → 55 nm). The convergence of the two methods on the same relative reduction is the strongest piece of quantitative evidence that the addition of CTAC genuinely halves the effective crystallite size of $BaCO_3$ under the present hydrothermal conditions.

3.2.4 Reflection-by-reflection comparison

To remove any residual ambiguity related to the choice of the reference peak, the reflections of the two samples were paired on the basis of their angular position (matching window of ± 0.5° in 2θ), and the Scherrer expression was applied to each pair. The result is summarised in Figure 4: in all fourteen matched reflections, ranging from 19.5° to 55.7°, the CTAC-treated sample exhibits a smaller crystallite size than the reference. The largest absolute differences are observed for the strongest reflections, where the FWHM increases from ≈ 0.09° to ≈ 0.50° at 23.97° and from ≈ 0.05° to ≈ 0.42° at 31.50°. The reflection-by-reflection analysis shows that peak broadening is observed across all matched reflections, indicating an overall reduction in crystallite size that is largely uniform across different lattice planes.

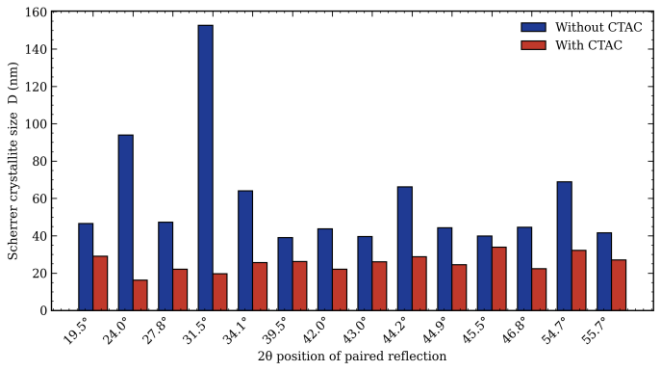

Figure 4. Reflection-by-reflection Scherrer crystallite size for the fourteen matched reflections of the two $BaCO_3$ samples

Notes: The systematic reduction of *D* over the whole 2θ range indicates that the broadening induced by CTAC is not selective for any particular crystallographic direction.

3.2.5 Preferred orientation (Harris texture coefficient)

The redistribution of the relative intensities noted in Section 3.1 was quantified by computing the Harris texture coefficient *TC(hkl)* for every paired reflection (Eq. (7)):

$$TC(hkl) = [I(hkl) / I_0(hkl)] \div [(1/N)\ \Sigma\ I(hkl)/I_0(hkl)] \qquad (7)$$

with the surfactant-free sample taken as the internal reference (I_0). Values of TC > 1 denote a preferential orientation along the corresponding plane, whereas TC < 1 reveals a relative suppression of the same plane. Harris' analysis provides its findings in Figure 5. The CTAC sample contains one large outlier at 23.88°, which reflects the (111) reflection with TC of roughly 6.5, while all other reflections fall below this threshold. CTA^+ preferentially adsorbs on (111) surface

regions, creating a larger barrier to development and resulting in plate-like crystallites as identified by FE-SEM.

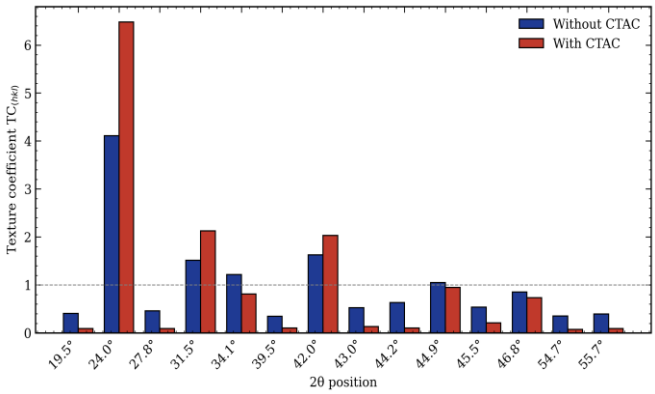

Figure 5. The Harris texture coefficient of the studied peaks for both phases of $BaCO_3$

3.2.6 Refinement of the orthorhombic witherite cell

Because $BaCO_3$ in the witherite phase belongs to the orthorhombic system ($a \neq b \neq c$, $\alpha = \beta = \gamma = 90°$), the inter-planar spacing is given by Eq. (8):

$$\frac{1}{d_{hkl}^2} = \frac{h^2}{a^2} + \frac{k^2}{b^2} + \frac{l^2}{c^2} \qquad (8)$$

The least-squares method was used to solve Eq. (8) by applying it to all indexed reflections of each pattern, which included sixteen reflections from the surfactant-free sample and eleven reflections from the CTAC sample, to determine the (*hkl*) indices. The fit is excellent for both samples (R^2 = 0.9989 and 0.9999, respectively), which confirms that the powders belong unambiguously to the witherite Pmcn structure. The refined lattice parameters of the surfactant-free sample, a = 5.287 Å, b = 8.926 Å, and c = 6.446 Å (V = 304.16 Å³), shift to a = 5.317 Å, b = 8.905 Å, and c = 6.453 Å (V = 305.53 Å³) on the addition of CTAC. The change is anisotropic: a expands by +30 mÅ (+0.57 %) and c by +7 mÅ (+0.11%), whereas b contracts by −21 mÅ (−0.23 %), and the cell volume increases by only +0.45%. This anisotropic deformation is best interpreted as the result of a directionally dependent surface stress imposed by the adsorbed CTA^+ layer, rather than as a homogeneous cell expansion. The values of a, b, and c are reported in Table 1. According to XRD analysis, barium carbonate nanostructure exhibits an orthorhombic crystal structure [27].

Table 1. Refined lattice parameters of the orthorhombic witherite cell (Pmcn) for the $BaCO_3$ samples synthesised with and without cetyltrimethylammonium chloride (CTAC)

Parameter	Without CTAC	With CTAC
a (Å)	5.287 ± 0.02	5.317 ± 0.02
b (Å)	8.926 ± 0.03	8.905 ± 0.03
c (Å)	6.446 ± 0.02	6.453 ± 0.02
Cell volume V (Å³)	304.16	305.53
Number of reflections used	16	11
Refinement R^2	0.9989	0.9999

3.2.7 Synthesis of the cetyltrimethylammonium chloride effect

It is useful, at this stage, to bring together the spectroscopic and the crystallographic evidence and to ask which physical processes can account for the changes that follow the addition of CTAC. Five mechanisms are usually invoked when a cationic surfactant modifies the crystallisation of an inorganic salt, and they are not mutually exclusive. The first mechanism is local enrichment of CO_3^{2-} around the micelles. Above the CMC, CTA^+ head groups attract carbonate and bicarbonate anions through electrostatic and weak hydrogen-bond interactions, so that the carbonate concentration close to a micelle is significantly higher than in the bulk solution [16, 28]. Our FTIR data are consistent with this picture: the small shifts and intensity changes of the ν_3 (1440 cm^{-1}) and ν_2 (860 cm^{-1}) carbonate bands in the CTAC sample reveal that the chemical environment of CO_3^{2-} is modified when the surfactant is present. The second mechanism is a higher nucleation rate. According to the LaMer hypothesis, a transitory rise in supersaturation causes a critical point, resulting in the production of small nuclei. This is the mechanism that is supported by the most evidence. The Halder-Wagner crystallite size decreases from 32 to 19 nm, dislocation density increases by more than one order of magnitude, and diffraction peaks broaden uniformly across the 2θ range. These characteristics indicate a higher number of smaller crystals rather than fewer larger crystals.

The third mechanism is a change in the interfacial energy. Adsorption of CTA^+ on a freshly formed $BaCO_3$ surface is expected to lower the solid–liquid interfacial tension and therefore to reduce the energy barrier to nucleation [29-31]. Our FTIR data give indirect support for this idea, because the C–H stretching bands at 2836 cm^{-1} confirm that CTA^+ is indeed present on the dried powder. We did not measure the interfacial tension directly, however, so this contribution remains qualitative.

The fourth mechanism is a soft-templating effect. Cationic micelles can guide the growth of an inorganic crystal towards specific facets [10, 15, 32]. The Harris analysis does show a clear preferential growth on (111) (TC ≈ 6.5), and FE-SEM reveals plate-like crystallites in the CTAC sample, both of which point in this direction. On the other hand, the broadening of all the matched reflections is essentially the same, which is not the behaviour expected from a strong, facet-selective template. We therefore consider the templating effect to be present but secondary. The fifth mechanism is a change in solubility induced by the surfactant counter-ions. Chloride and Ba^{2+} can form weak ion pairs, and the additional ionic strength produced by the surfactant can, in principle, modify the apparent solubility of $BaCO_3$ [33]. We did not measure the residual barium concentration in the supernatant, so we have no direct evidence for or against this mechanism. It is mentioned here only for completeness. In short, the dominant effect of CTAC under the present conditions is to increase the nucleation rate by enriching CO_3^{2-} at the micellar surface, with a smaller contribution from interfacial-energy lowering and from a mild orientation of the crystallites along (111). A solubility-driven effect cannot be ruled out, but it is not needed in order to explain the present results.

The FTIR and XRD data establish a coherent causal sequence that links the molecular-level interaction of CTA^+ with the carbonate surface to the macroscopic crystallographic changes measured by diffraction. The FTIR spectrum of the CTAC-treated sample shows (i) a shift and intensity change of the ν_3 carbonate band at ~1440 cm^{-1} and of the ν_2 band at ~860 cm^{-1}, indicating that the CTA^+ head group interacts electrostatically with CO_3^{2-} ions, and (ii) C–H stretching band at 2836 cm^{-1} region that confirm the retention of the cetyl

chain on the dried powder, demonstrating that CTA^+ is indeed adsorbed on the $BaCO_3$ surface and is not simply present as a dissolved species in the mother liquor. This surface adsorption has three direct crystallographic consequences that are all observed in the XRD data. First, the electrostatic enrichment of CO_3^{2-} at the micelle surface leads to increased local supersaturation, which results in a LaMer-type nucleation burst that produces more crystallites while decreasing their average size from approximately 94 nanometers to approximately 55 nanometers based on the single-peak Scherrer method and from approximately 32 nanometers to approximately 19 nanometers based on the Halder-Wagner method. Second, the adsorption of CTA^+ lowers the solid–liquid interfacial energy, which further reduces the nucleation barrier and drives the thirteen-fold rise in dislocation density (δ: 1.79 to 23.72 × 10^{14} lines·m^{-2}) associated with the finer, grain-boundary-rich microstructure. Third, the preferential adsorption of CTA^+ on specific $BaCO_3$ facets retards growth along those directions and produces the strong preferred orientation along the (111) plane detected by the Harris texture analysis (TC ≈ 6.5). In other words, the FTIR features at 1440, 860, and 690 cm^{-1} are the standard ν_3, ν_2, and ν_4 vibrations of the carbonate group in witherite $BaCO_3$ and confirm the phase identity already inferred from XRD. The noticeable reduction in the intensity of these bands when CTAC is present is consistent with surface coverage of the $BaCO_3$ crystallites by adsorbed CTA^+, which screens the carbonate vibrations from the IR beam. This surface coverage is also the most likely reason why the XRD peaks of the CTAC sample are slightly broader (smaller crystallite size) than those of the surfactant-free sample, since adsorbed CTA^+ limits further growth.

The SEM pictures in Figure 6 show that the morphology and form of the nanoparticles had changed. As seen in Figure 6(a), the nanoparticles' appearance was highly erratic prior to the incorporation of the CTAC. The morphology altered to a well-distributed one after the CTAC was added (Figure 6(b)). Because the CTA+ ions have a positive charge throughout crystallization, preferential bonding is viewed between them and the $BaCO_3$ surfaces. The energy of the crystal surfaces and, as a result, the rate at which different crystallographic directions crystallize are influenced by preferred bonding. The shape of the crystalline structures is altered as some crystallographic planes grow more slowly than others. Consequently, the use of the CTAC solution leads to the creation of micelles that include some of the Ba^{2+} ions. Consequently, the local supersaturation near the micellar surface is enhanced, triggering a burst of nucleation events and producing a larger number of smaller crystallites. The size dispersion and shape of the crystallites improve when ions are adsorbed onto their surface. It should be noted that the information shown in Table 1 and Figure 2 is consistent with the results indicated. CTAC and CTAB are popular surfactants that have been used extensively to regulate the shape and growth of numerous inorganic compounds, aside from their function in the $BaCO_3$ system.

According to the analysis's findings, it is evident that the $BaCO_3$ crystals' lamellar morphology is a result of CTAC, which encourages molecules to diffuse while maintaining their original structure and shape, hence fostering optimal molecular performance. FTIR, XRD, and SEM clearly show that CTAC has a significant impact on the molecular structure and morphology of $BaCO_3$. Additionally, the usage of CTAC can be linked to improvements in the characteristics of $BaCO_3$, as seen by the differences in the diffraction peaks in the XRD spectra and absorption peaks in the FTIR spectrum, as well as the improved SEM pictures acquired. As a result, the content will become more engaging for practical uses. In summary, the study's findings pave the way for additional research into the potential applications of CTAC as an agent that permits manipulation of nanomaterials' characteristics, especially those of nanoceramics. Increased particle contact will lead to better crystallization. As a result, the samples will be closely packed and have a more uniform structure.

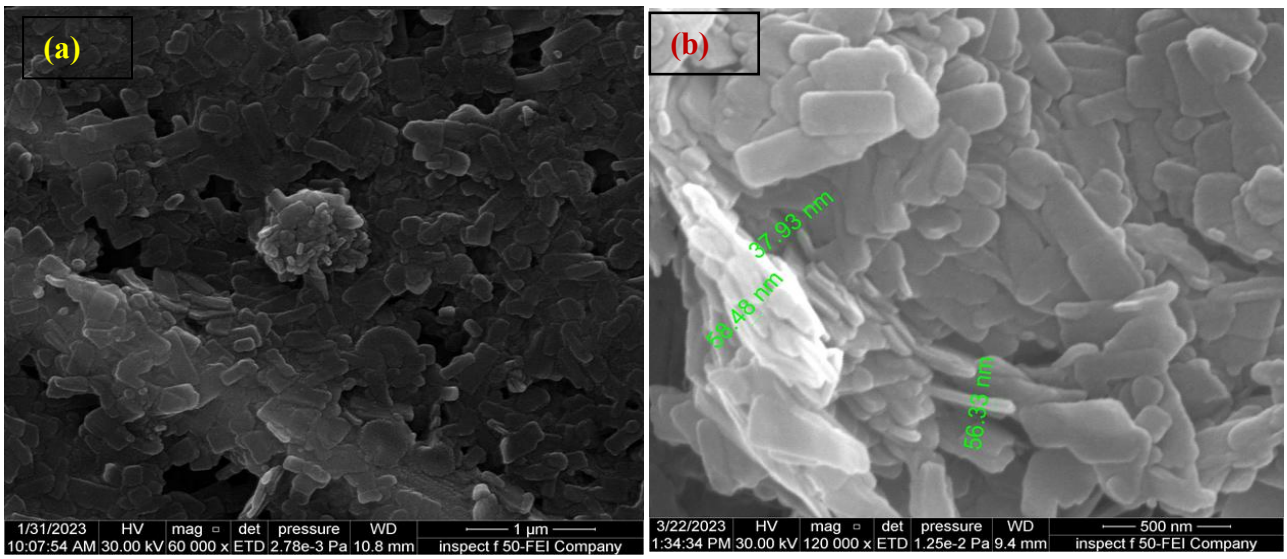

Figure 6. The FE-SEM images of barium carbonate (a) in the absence of CTAC, (b) in the presence of CTAC
Notes: FE-SEM: Field emission scanning electron microscopy, CTAC: Cetyltrimethylammonium chloride.

3.2.8 Mie-theory optical simulation

To assess how the CTAC-induced reduction in crystallite size translates into measurable optical behaviour, the extinction efficiency Q_e, scattering efficiency Q_s, specific extinction cross-section per unit mass, and scattering asymmetry parameter g were computed by exact Mie theory for spherical $BaCO_3$ particles with diameters equal to those determined by single-peak Scherrer analysis: $D_1 = 94$ nm (surfactant-free) and $D_2 = 55$ nm (CTAC-treated). The refractive index of the witherite phase was represented by a

three-term Cauchy model.

$$n(\lambda) = 1.630 + 0.0122\lambda^{-2} + 4.2 \times 10^{-4}\lambda^{-4} \ (\lambda \text{ in } \mu m)$$

with parameters fitted to published optical data for the mineral witherite. Since $BaCO_3$ is optically transparent across the ultraviolet–visible spectrum (imaginary part of the refractive index $k \approx 0$), the absorption efficiency is essentially zero in both samples, and all extinction arises from elastic Mie scattering.

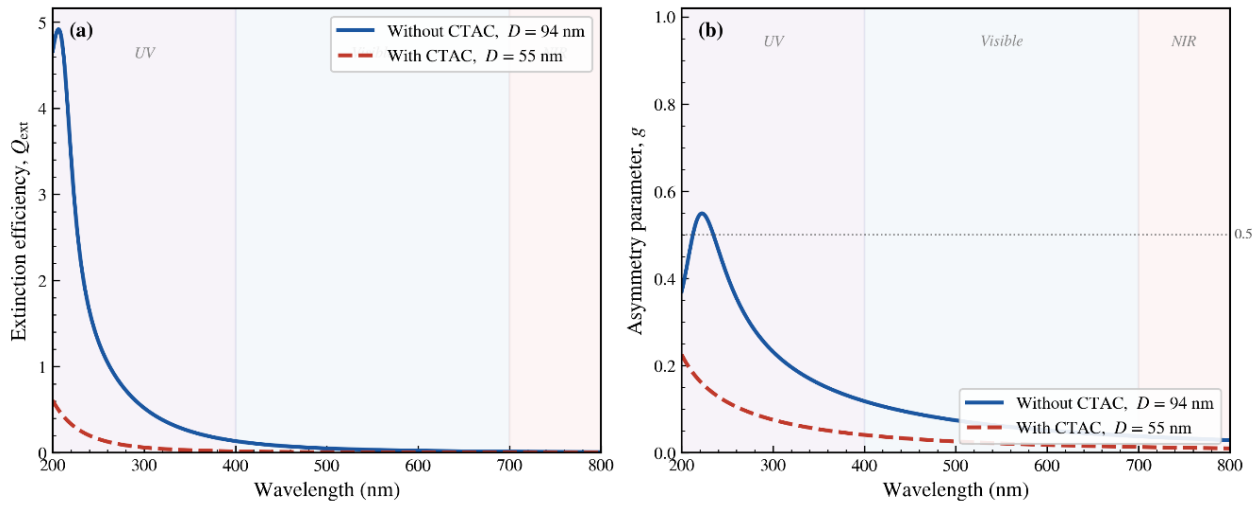

Figure 7. The optical efficiencies of $BaCO_3$ particles synthesized without cetyltrimethylammonium chloride (CTAC) (D = 94 nm, solid blue line) and with CTAC (D = 55 nm, dashed red line): (a) extinction efficiency Q_e, (b) scattering asymmetry parameter g

Notes: Shaded regions indicate the UV (violet), visible (blue), and near-IR (pale red) spectral ranges.

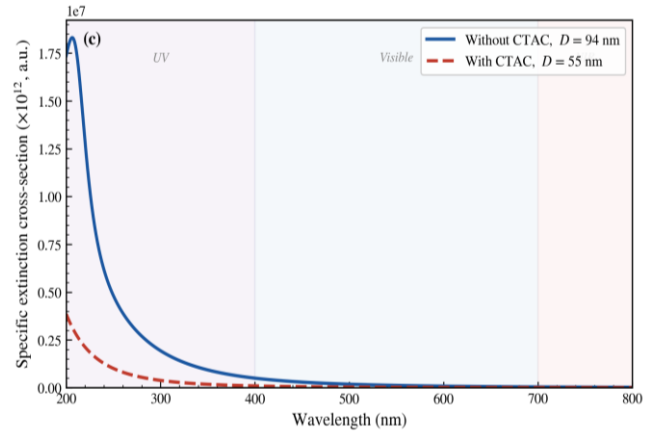

Figure 8. Specific extinction cross-section per unit mass ($C_e/m = 3Q / 4\rho r \times 10^{12}$ cm^2/g) as a function of wavelength for the two $BaCO_3$ samples

Notes: The surfactant-free powder (94 nm) shows higher UV extinction per gram, while the cetyltrimethylammonium chloride (CTAC)-treated powder (55 nm) has a flatter spectral response across the full UV–visible window.

The computed extinction efficiencies are shown in Figure 7(a) The surfactant-free sample, whose larger particle size (94 nm) places it in the Mie-resonance regime for wavelengths below 350 nm, exhibits a pronounced extinction peak in the deep UV with Q_e reaching values above 1.1; by contrast, the CTAC-treated sample (55 nm) remains in the Rayleigh–Mie transition throughout this range and shows a mean UV extinction of only 0.121. In the visible range (400–700 nm), where both samples are nearly transparent, the CTAC-treated powder exhibits an 88.7% lower mean Q_e (0.0050 versus 0.0445), indicating that the finer particles scatter visible light less efficiently, a property of direct relevance to transparent ceramic glazes and optical-grade coatings. The visible range scattering asymmetry parameter g decreases from 0.066 (no CTAC) to 0.023 (CTAC) as measured between these two sites, as shown in Figure 7(b). A lower g value correlates to greater isotropic angular redistribution of scattered intensity, resulting in a more uniform look that reflects light, as seen in white ceramic glazes and diffuse optical coatings. Figure 8 depicts the specific extinction cross-section normalized by particle mass, $C_e / m = 3Q_e / (4\rho r)$, where $\rho = 4.286$ g cm^{-3} is the bulk density of witherite and r is the particle radius. The quantity serves as the optimal measurement to assess the optical efficiency between two powders that will be tested at identical mass loading in a formulation. The surfactant-free sample exhibits higher specific UV extinction because its bigger resonant particles eliminate more UV light from the incoming beam per gram of material. Mie-theory studies reveal that reducing crystallite size from 94 nm to 55 nm causes the optical response to change from significant UV scattering to better visible transparency and more isotropic light distribution, rather than simply increasing or deteriorating performance.

4. CONCLUSION

The incorporation of CTAC into the $BaCO_3$ hydrothermal synthesis method produced two significant consequences. The first result revealed that the average crystallite size fell from 94 to 55 nanometers. The second finding demonstrated that increasing dislocation density resulted in a more uniform plate-like structure. Instead of being a typical crystallinity-enhancing agent, CTAC acts as a nucleation promoter and surface-adsorption agent, resulting in these results. XRD study shows that CTAC addition generates peak widening effects, resulting in novel patterns of diffraction intensity distribution that correlate to smaller average crystallite sizes. As shown in the XRD pattern, when CTAC was introduced, there was a redistribution of peak intensities accompanied by increased

peak broadening, consistent with the reduction in crystallite size. The Scherrer equation was applied to quantify the CTAC-induced reduction in crystallite size. Furthermore, there was also a shift of functional groups and their absorptions according to FTIR spectra after the introduction of CTAC. SEM images have revealed that particles are uniform and homogeneously dispersed. The Scherrer equation confirmed the CTAC-induced reduction in crystallite size, thereby demonstrating the suitability of employing CTAC as an additive for controlling the crystallinity and morphology of $BaCO_3$ in various applications. The production of laminated $BaCO_3$ particles with the help of CTAC is very important from the point of view of the industrial process, as this particular form is known to be more suitable for obtaining an interfacial contact space between the reactants, and thus will promote the crystallization reaction. These findings will improve condensation efficiency and produce more uniform ceramic materials. The two-dimensional lamellar crystal structure has a very precise thickness and a large surface area. Its crystalline surfaces are primarily exposed, thereby enhancing this structure's efficacy. Due to their enhanced capacity for charge and mass transfer, these structures have certain benefits that make them indispensable in situations involving chemical catalysis, sensing, and electronics [19]. To validate and visualise the experimental line-profile data, XRD patterns were simulated for both samples using the Scherrer–Voigt broadening model with the crystallite sizes and microstrain values obtained from the Williamson–Hall analysis (D = 94 nm, $\varepsilon = 0.95 \times 10^{-3}$ without CTAC; D = 55 nm, $\varepsilon = 1.12 \times 10^{-3}$ with CTAC). The simulated patterns reproduce the systematic peak broadening observed experimentally across all fourteen matched reflections and confirm that the strain-induced broadening term $4\varepsilon \tan\theta$ becomes increasingly significant at high angles ($2\theta > 45°$), explaining the gradual divergence of the two profiles. Critically, the simulation demonstrates that the redistribution of relative peak intensities seen in the CTAC sample cannot be reproduced by crystallite-size reduction alone: an additional preferential-orientation contribution—independently confirmed by the Harris texture coefficient (TC ≈ 6.5 at the (111) reflection)—is required to match the experimental intensity ratios. The simulation, therefore, provides a self-consistent, quantitative bridge between the crystallographic analysis and the FE-SEM morphological observations, and strengthens the conclusion that CTAC acts primarily as a nucleation regulator with a secondary facet-selective orientation effect on the (111) plane. Barium carbonate nanostructures were successfully synthesised by a hydrothermal route in the absence and presence of CTAC, and a complete crystallographic and microstructural analysis was carried out by FTIR, FE-SEM, and XRD. Single-peak Scherrer estimates yielded average crystallite sizes of approximately 94 nm and 55 nm for the two samples, while averaging over the ten most intense reflections returned 43 nm and 34 nm. The Williamson–Hall and the Halder–Wagner size–strain treatments confirmed that the addition of CTAC reduces the average crystallite size by a factor close to two (32 to 19 nm). Least-squares refinement of the orthorhombic witherite cell ($R^2 \geq 0.9989$) showed that the cell deformation induced by CTAC is anisotropic (a and c expand, b contracts) rather than a uniform expansion, and the Harris texture analysis revealed a strong preferential orientation along the (111) plane (TC ≈ 6.5). FE-SEM confirmed the corresponding morphological refinement, with the irregular agglomerates of the surfactant-free reference being replaced by homogeneous, plate-like crystallites in the CTAC sample. The Mie-theory simulation demonstrates that decreasing the crystallite size from 94 nanometers to 55 nanometers produces a substantial change in the optical characteristics of $BaCO_3$. The material demonstrates a transition from intense ultraviolet scattering to enhanced visible light transmission and even distribution of light. CTAC functions mainly as the primary nucleation agent, while it fails to control crystal shape development, which results in the production of uniformly structured fine powder that serves as a suitable precursor for ceramic production. The study used only one CTAC concentration of 6.25 mM, which exceeds the critical micelle concentration, yet it represents only one concentration value. The results show system behavior at this particular condition, while researchers did not determine the ideal CTAC concentration. Future research should use a systematic concentration-gradient study that covers sub-CMC, near-CMC, and supra-CMC regimes to establish how crystallite size, morphology, and texture depend on surfactant loading.

REFERENCES

[1] Abidine, B., Yahya, M., Mhadhbi, M., Bouzidi, C., Hamzaoui, A.H. (2022). Characterization and luminescence properties of Eu3+ doped BaCO3 nanoparticles synthesized by autocombustion method. Journal of Molecular Structure, 1263: 133122. https://doi.org/10.1016/j.molstruc.2022.133122

[2] Ehab, M., Salama, E., Ashour, A., Attallah, M., Saleh, H.M. (2022). Optical properties and gamma radiation shielding capability of transparent barium borosilicate glass composite. Sustainability, 14: 13298. https://doi.org/10.3390/su142013298

[3] Zelati, A., Amirabadizadeh, A., Kompany, A. (2011). Preparation and characterization of barium carbonate nanoparticles. International Journal of Chemical Engineering and Applications, 2(4): 299.

[4] Manzoor, U., Kim, D.K. (2007). Synthesis of nano-sized barium titanate powder by solid-state reaction between barium carbonate and titania. Journal of Materials Science & Technology, 23: 655-658.

[5] Apaydin, F., Tunç Parlak, T., Yıldız, K. (2019). Low temperature formation of barium titanate in solid state reaction by mechanical activation of BaCO3 and TiO2. Materials Research Express, 6(12): 126330. https://doi.org/10.1088/2053-1591/ab6c0d

[6] Inam, F., Heaton, A., Brown, P., Peijs, T., Reece, M.J. (2014). Effects of dispersion surfactants on the properties of ceramic–carbon nanotube (CNT) nanocomposites. Ceramics International, 40(1): 511-516. https://doi.org/10.1016/j.ceramint.2013.06.031

[7] Kohli, P.S., Devi, P., Reddy, P., Raina, K.K., Singla, M.L. (2012). Synthesis and electrical behavior study of Mn3O4 nanoceramic powder for low temperature NTC thermistor. Journal of Materials Science: Materials in Electronics, 23(10): 1891-1897. https://doi.org/10.1007/s10854-012-0680-2

[8] Wu, W., Zhang, L., Zhai, X., Liang, C., Yu, K. (2018). Preparation and photocatalytic activity analysis of nanometer TiO2 modified by surfactant. Nanomaterials and Nanotechnology, 8: 1847980418781973. https://doi.org/10.1177/1847980418781973

[9] Chen, J., Fan, Z., Zhou, H., Cui, Y., Chen, S., Kuang, Y. (2020). Impact of surfactant on the synthesis and dispersion of zinc oxide nanoparticles. Journal of Hunan University (Natural Sciences), 31(6): 1-5.

[10] Naik, S.P., Elangovan, S.P., Okubo, T., Sokolov, I. (2007). Morphology control of mesoporous silica particles. The Journal of Physical Chemistry C, 111(30): 11168-11173. https://doi.org/10.1021/jp072184a

[11] Moon, S.Y., Kusunose, T., Sekino, T. (2009). CTAB-assisted synthesis of size-and shape-controlled gold nanoparticles in SDS aqueous solution. Materials Letters, 63(23): 2038-2040. https://doi.org/10.1016/j.matlet.2009.06.047

[12] Khan, Z., Singh, T., Hussain, J.I., Hashmi, A.A. (2013). Au (III)–CTAB reduction by ascorbic acid: Preparation and characterization of gold nanoparticles. Colloids and Surfaces B: Biointerfaces, 104: 11-17. https://doi.org/10.1016/j.colsurfb.2012.11.017

[13] Shahid, T., Arfan, M., Zeb, A., BiBi, T., Khan, T.M. (2018). Preparation and physical properties of functional barium carbonate nanostructures by a facile composite-hydroxide-mediated route. In Nanomaterials and Nanotechnology. https://doi.org/10.1177/1847980418761775

[14] Mishra, S.K., Tripathi, U.K., Awasthi, R.R., Shukla, R.K., Kumar, I., Naik, R.M., Mishra, D.P. (2021). CTAB mediated synthesis of ZnO nanoparticles: Structural, optical and enhanced blue-green optical emission. Materials Today: Proceedings, 46: 2229-2234. https://doi.org/10.1016/j.matpr.2021.03.481

[15] Ohkubo, T., Ogura, T., Sakai, H., Abe, M. (2007). Synthesis of highly-ordered mesoporous silica particles using mixed cationic and anionic surfactants as templates. Journal of Colloid and Interface Science, 312(1): 42-46. https://doi.org/10.1016/j.jcis.2007.02.043

[16] Li, D., Li, H., Fu, Y., Zhang, J.L., Li, W., Han, Y.C., Wang, L. (2008). Critical micelle concentrations of cetyltrimethylammonium chloride and their influence on the periodic structure of mesoporous silica. Colloid Journal, 70(6): 747-752. https://doi.org/10.1134/S1061933X08060100

[17] Kim, J., Martin, O.J. (2023). Trap-and-track for characterizing surfactants at interfaces. Molecules, 28(6): 2859. https://doi.org/10.3390/molecules28062859

[18] Wang, X., Zhang, Y., Zhi, R., Yang, S., Hu, X., Wang, Y. (2018). Surface activity, micellization properties and aggregation behavior of cetyltrimethylammonium chloride/sodium dodecyl benzene sulfonate mixtures. Journal of Molecular Liquids, 263: 419-427. https://doi.org/10.1016/j.molliq.2018.05.019

[19] Mukerjee, P., Mysels, K.J. (1971). Critical micelle concentrations of aqueous surfactant systems. NSRDS-NBS 36, U.S. National Bureau of Standards. https://doi.org/10.6028/NBS.NSRDS.36

[20] Kuperkar, K., Abezgauz, L., Danino, D., Verma, G., Hassan, P.A., Aswal, V.K., Varade, D., Bahadur, P. (2008). Viscoelastic micellar water/CTAB/NaNO3 solutions: Rheology, SANS and cryo-TEM analysis. Journal of Colloid and Interface Science, 323(2): 403-409. https://doi.org/10.1016/j.jcis.2008.04.040

[21] Atkin, R., Craig, V.S.J., Wanless, E.J., Biggs, S. (2003). Mechanism of cationic surfactant adsorption at the solid–aqueous interface. Advances in Colloid and Interface Science, 103(3): 219-304. https://doi.org/10.1016/S0001-8686(03)00002-2

[22] Ye, S., Brown, A.P., Stammers, A.C., Thomson, N.H., Wen, J., Roach, L., Bushby, R.J., Coletta, P.L., Critchley, K., Connell, S.D., Markham, A.F., Brydson, R., Evans, S.D. (2019). Sub-nanometer thick gold nanosheets as highly-efficient catalysts. Advanced Science, 6(21): 1900911. https://doi.org/10.1002/advs.201900911

[23] Desta, H.G., Yang, Q., Tian, D., Zhu, S., et al. (2022). BaCO3 nanoparticles-modified composite cathode with improved electrochemical oxygen reduction kinetics for high-performing ceramic fuel cells. Catalysts, 12(9): 1046. https://doi.org/10.3390/catal12091046

[24] Zavabeti, A., Jannat, A., Zhong, L., Haidry, A.A., Yao, Z., Ou, J.Z. (2020). Two-dimensional materials in large-areas: Synthesis, properties and applications. Nano-Micro Letters, 12(1): 66. https://doi.org/10.1007/s40820-020-0402-x

[25] Lin, J., Zhou, W., O'Connor, C.J. (2001). Formation of ordered arrays of gold nanoparticles from CTAB reverse micelles. Materials Letters, 49(5): 282-286. https://doi.org/10.1016/S0167-577X(00)00385-2

[26] Sreedhar, B., Vani, C.S., Devi, D.K., Rao, M.B., Rambabu, C. (2012). Shape controlled synthesis of barium carbonate microclusters and nanocrystallites using natural polysachharide–gum Acacia. American Journal of Materials Science, 2(1): 5-13. https://doi.org/10.5923/j.materials.20120201.02

[27] Alavi, M.A., Morsali, A. (2008). Syntheses of BaCO3 nanostructures by ultrasonic method. Ultrasonics Sonochemistry, 15(5): 833-838. https://doi.org/10.1016/j.ultsonch.2008.02.006

[28] De Yoreo, J.J., Vekilov, P.G. (2003). Principles of crystal nucleation and growth. Reviews in Mineralogy and Geochemistry, 54(1): 57-93. https://doi.org/10.2113/0540057

[29] LaMer, V.K., Dinegar, R.H. (1950). Theory, production and mechanism of formation of monodispersed hydrosols. Journal of the American Chemical Society, 72(11): 4847-4854. https://doi.org/10.1021/ja01167a001

[30] Thanh, N.T.K., Maclean, N., Mahiddine, S. (2014). Mechanisms of nucleation and growth of nanoparticles in solution. Chemical Reviews, 114(15): 7610-7630. https://doi.org/10.1021/cr400544s

[31] Cölfen, H., Mann, S. (2003). Higher-order organization by mesoscale self-assembly and transformation of hybrid nanostructures. Angewandte Chemie International Edition, 42(21): 2350-2365. https://doi.org/10.1002/anie.200200562

[32] Qi, L., Cölfen, H., Antonietti, M. (2000). Crystal design of barium sulfate using double-hydrophilic block copolymers. Angewandte Chemie International Edition, 39(3): 604-607. https://doi.org/10.1002/(SICI)1521-3773(20000204)39:3%3C604::AID-ANIE604%3E3.0.CO;2-B

[33] Söhnel, O., Garside, J. (1992). Precipitation: Basic Principles and Industrial Applications. Butterworth-Heinemann, Oxford, UK.